Fuzzy-Adaptive Super-Twisting Sliding Mode Observer for Sensorless Permanent Magnet In-Wheel Motor Control in Electric Vehicles

Hao Huang, Sai Wang, Chunfeng Yu, Zhonghua Sun, Yuanfeng Zhang, and Keqin Li, *Fellow, IEEE*

***Abstract*— This article introduces an innovative sensorless control methodology for permanent magnet in-wheel motors (PMIWMs) in distributed-drive electric vehicles (DDEVs). First, a disturbance boundary estimation technique is integrated to increase the system's robustness against external perturbations and parameter uncertainties. Second, a fuzzy-adaptive super-twisting sliding mode observer (FSTSMO) is developed to mitigate the challenges of chattering and infinite-time convergence commonly associated with traditional sliding mode observers (SMOs). This hybrid framework leverages fuzzy inference mechanisms to adaptively tune the switching gains in real-time, thereby ensuring finite-time convergence while substantially reducing chattering phenomena. Third, a phase-locked loop (PLL) is incorporated within the observer architecture to enhance the accuracy of the rotor position estimation through dynamic phase synchronization. Extensive simulations alongside hardware-in-the-loop experiments validate that the proposed FSTSMO-PLL approach, combined with disturbance boundary estimation, achieves rapid command tracking and reduced speed error relative to conventional SMOs. In particular, the control strategy maintains stable motor performance during acceleration and dynamic load variations without dependence on physical speed sensors, providing a cost-efficient and dependable sensorless solution for PMIWM-driven DDEVs, especially suited for operation in challenging environments or scenarios with limited installation space.**

***Index Terms*— Fuzzy controller, phase-lock loop, sensorless control, super-twisting sliding mode controller.**

I. Introduction

RECENTLY, distributed-drive electric vehicles (DDEVs) equipped with permanent magnet in-wheel motors (PMIWMs) have garnered significant attention in global automotive research. Compared to conventional centralized-drive electric vehicles (CDEVs), PMIWM-based DDEVs eliminate the mechanical transmission components, such as clutches and transmission shafts, thereby simplifying powertrain architectures and enhancing energy transfer efficiency [1], [2]. In addition, the ability of PMIWMs to control torque separately allows for better steering and management of how the vehicle moves, providing improved handling and flexibility [3], [4]. These inherent advantages position PMIWM-driven DDEVs as a transformative choice for future electric vehicles, particularly in scenarios requiring compact design and adaptable movement control in constrained spaces.

Currently, sensors are commonly installed in the PMIWM, which can monitor and provide feedback on the speed signal to enhance the control precision [5]. However, this component can increase vehicles' unsprung mass and reduce their reliability when working in a harsh environment. In addition, installing sensors causes defects that raise the cost of the control system [6], [7]. Therefore, the adoption of sensorless control for PMIWM is crucial.

The sliding mode observer (SMO) is widely used for controlling motors without sensors because it can handle disturbances well, does not depend on specific parameters, and responds quickly [8]. However, two inherent defects limit the further improvement of this method. The first is the chattering problem caused by nonlinear control, and the second is the infinite-time convergence problem caused by the linear sliding mode surface [9].

Aiming at the issue of chattering value, in [10], a new strategy for compensating disturbance observers is proposed using the compound reaching law (CRL). While this method reduces chattering, it imposes a computational strain due to its intricate reaching law. In [11], an adaptive SMO is addressed to decrease chattering amplitude. However, the sliding mode gain approaches zero as the control deviation diminishes, negatively impacting the control system. An exponential convergence method in direct torque control is shown in [12], which can improve system stability and reduce chattering. While such algorithmic approaches demonstrate theoretical advantages, their implementation inevitably incurs elevated computational overhead in control systems. To address this challenge, recent developments in observer-based control theory have been presented in [13], which effectively suppresses high-frequency chattering in drive systems. However, this enhanced dynamic performance decreases system tolerance to parameter variations. In addition, Zhang et al. [14] proposed a finite-time SMO approach to resolve the chattering issue. However, this method lacks precision in adjusting control parameters across various systems.

Tackling the issue of infinite-time convergence, in [15], a novel control scheme integrating finite-time convergence theory with SMO was conceived. Based on nonlinear control theory, this approach significantly enhances steady performance

Received 25 September 2025; revised 5 November 2025; accepted 1 December 2025. Date of publication 4 December 2025; date of current version 25 March 2026. This work was supported in part by the National Key Research and Development Program of China under Grant 2016YFC0802903 and in part by the National Natural Science Foundation of China under Grant 61671470. *(Corresponding author: Keqin Li.)*

Hao Huang, Sai Wang, Chunfeng Yu, Zhonghua Sun, and Yuanfeng Zhang are with Naval Aeronautical University, Qingdao Campus, Qingdao 266000, China (e-mail: haohuang_130@whu.edu.cn).

Keqin Li is with the Department of Computer Science, State University of New York, New Paltz, NY 12561 USA (e-mail: lik@newpaltz.edu).

Digital Object Identifier 10.1109/TTE.2025.3640616

and quick reactions for motor drive systems facing variable conditions. Nevertheless, it encounters singularity challenges. The adaptive nonsingular fast SMO in [16], using a nonlinear saturation function to ensure errors quickly decrease on sliding surfaces. However, the control law includes discontinuous switching functions, potentially causing oscillations in the control system. An enhanced sliding mode control framework with nonlinear convergence dynamics was proposed in [17], facilitating a direct drive system's high speed, precise movements. This advanced control architecture demonstrates faster convergence rates than conventional terminal sliding mode approaches while eliminating singularity phenomena common in high-order systems operating under inertial coupling conditions. However, the complexity of this SMO algorithm results in a considerable computational load on the processor. In [18], a new sliding mode observation system was introduced that uses global finite-time convergence theory to improve errors and lessen chattering. However, the control parameters remain constant, preventing ideal real-time control performance optimization.

Compared to the previously mentioned SMO methods, the super-twisting SMO (STSMO) has emerged as a superior candidate for sensorless control applications. This design removes sudden changes, reduces chattering, and ensures that errors decrease in a limited time using nonlinear sliding surfaces [19], [20]. The STSMO operates by introducing an additional integral term into the control law. This unique structure allows it to directly act on the higher order time derivatives of the sliding variable, effectively suppressing the chattering while preserving the paramount robustness properties of the standard SMO. Specifically, the continuous control output of the STSMO is generated from a discontinuous function acting underneath the integration process, which smooths out the output and eliminates high-frequency switching. In addition, the computational requirements of this method are relatively low.

In [20], an STSMO method was designed to realize chattering avoidance via continuous control. In [21], an adaptive-gain STSMO was proposed to balance estimation accuracy and the chattering problem. A STSMO with a complex vector generalized integrator for sensorless control of a motor is proposed in [22], which can realize the compromise between chattering and estimation accuracy under limited control frequency in practice.

However, implementing a sensorless control technique based on existing STSMO has two common issues. First, the unmodeled disturbances of SMO will amplify observation errors, causing state estimation values to deviate from their actual values, resulting in steady-state errors or accuracy fluctuations that seriously affect the stability of the observer [23], [24]. In [25], a novel barrier function-based adaptive sliding mode control (BFASM) scheme can handle input saturation and uncertainties without requiring the upper bound of the disturbance, ensuring a stable state of the closed-loop system within a predetermined area. Based on this method, we aim to resolve the inherent trade-off between convergence speed and chattering caused by inappropriate parameter selection.

A novel BFASM scheme can handle input saturation and uncertainties without requiring the upper bound of the disturbance, ensuring a stable state of the closed-loop system within a predetermined area. Based on this method, we aim to resolve the inherent trade-off between convergence speed and chattering caused by inappropriate parameter selection. This research systematically organizes its principal innovations as follows.

1) An unmodeled disturbance estimation method is adopted to determine the boundary value of disturbance in real-time, which provides a theoretical basis for a precise and adaptive sliding mode gain, thereby overcoming the traditional conservative gain selection and improving control precision.
2) An STSMO is developed to supercede conventional SMO frameworks. Employing a higher order sliding mode algorithm effectively suppresses the high-frequency switching chattering inherent in conventional SMOs while maintaining the robustness and finite-time convergence properties.
3) An adaptive fuzzy logic module is integrated with the STSMO architecture, enabling real-time parameter regulation to optimize closed-loop performance metrics.

This research adopts the following organizational framework. Section II formulates the mathematical framework of PMIWMs with disturbance-bound estimation in the rotating reference frame. Section III introduces an integrated design paradigm combining STSMO with fuzzy parameter adaptation mechanisms. Section IV systematically validates the sensorless control architecture through comparative simulations and experimental tests on a motor-inverter test bench. Section V highlights the main technical advancements in designing nonlinear observers and suggests three new research directions for future sensorless drive systems.

II. Modeling of PMIWM

The main subject of this study is the high-performance control techniques of the exterior rotor inside PMIWM for electric vehicle propulsion under various operating conditions. As illustrated in Fig. 1, the motor features a 25-slot stator and 24-pole rotor configuration with 40 mm axial length, employing a circumferential magnetization topology for embedded permanent magnets. This compact architecture achieves high torque density while optimizing rare-earth material utilization, making it particularly suitable for space-constrained automotive applications. The mathematical modeling of PMIWM incorporates these fundamental assumptions [26], [27]: 1) the effects of iron core saturation are ignored; 2) magnetic circuit linearity is presumed; 3) motor inductance parameters remain invariant; 4) eddy current and hysteresis losses are excluded; 5) rotor magnetic fields exhibit sinusoidal airgap distribution with balanced three-phase sinusoidal currents; and 6) rotor damping windings are absent. Under these premises, the following equation describes the derived PMIWM dynamics in the synchronous rotating coordinate system:

$$\frac{d}{dt}\begin{bmatrix} i_\alpha \\ i_\beta \end{bmatrix} = -\frac{R}{L_s}\begin{bmatrix} i_\alpha \\ i_\beta \end{bmatrix} + \frac{1}{L_s}\begin{bmatrix} u_\alpha \\ u_\beta \end{bmatrix} - \frac{1}{L_s}\begin{bmatrix} e_\alpha \\ e_\beta \end{bmatrix} - \begin{bmatrix} d_\alpha \\ d_\beta \end{bmatrix} \quad (1)$$

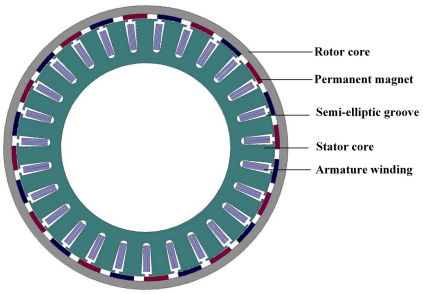

Fig. 1. Structure of PMIWM.

where the currents of the α/β axis are represented by i_α and i_β, respectively. The resistance is represented by R; the inductance of the d/q axis is represented by L_s, respectively; the voltages of the α/β axis are represented by u_α and u_β, respectively. The back electromotive forces (BEFs) of the α/β axis are represented by E_α and E_β, respectively. d_α and d_β are disturbances.

Denote $X_1 = \begin{bmatrix} i_\alpha & i_\beta \end{bmatrix}^{\mathrm{T}}$, $U = \begin{bmatrix} u_\alpha & u_\beta \end{bmatrix}^{\mathrm{T}}$, $E = \begin{bmatrix} e_\alpha & e_\beta \end{bmatrix}^{\mathrm{T}}$, and $D = \begin{bmatrix} d_\alpha/L_s & d_\beta/L_s \end{bmatrix}^{\mathrm{T}}$, D is unknown but is a bounded function with $\max\{|d_\alpha/L_s|, |d_\beta/L_s|\} < l$, l is the bound. Equation (1) can be extended to the following dynamical systems:

$$L_s \dot{X}_1 = (-RX_1 + U + E) - D. \tag{2}$$

In this article, the parameter uncertainties are considered to satisfy

$$\begin{cases} L_s = L_{s0} + \Delta L_s \\ R = R_0 + \Delta R \end{cases} \tag{3}$$

where L_{s0} and R_0 represent the initial value of L_s and R, and ΔL_s and ΔR represent the uncertain value of L_s and R, denote

$$\begin{cases} \Delta L_s \le r_1 \\ \Delta R \le r_2. \end{cases} \tag{4}$$

By substituting (3) into (2), we can obtain

$$L_{s0}\dot{X}_1 = (-R_0 X_1 + U + E) + \delta \tag{5}$$

where $\delta = -D - \Delta R X_1 - \Delta L_s \dot{X}_1$ represents the reformatted uncertainty in the system. From (2) to (5), we can obtain

$$\begin{aligned} |\delta| &= \left|-D - \Delta R X_1 - \Delta L_s \dot{X}_1\right| \\ &\le |D| + |\Delta R X_1| + \left|\Delta L_s \dot{X}_1\right| \\ &\le l + r_2|X_1| + r_1 L_s^{-1}|-(R_0 + \Delta R)X_1 + U + E - F| \\ &\le l + r_2|X_1| + r_1 L_{s0}^{-1}((R_0 + r_2)|X_1| + |U| + |E| + l) \\ &= \left(r_2 + r_1 L_{s0}^{-1}(R_0 + r_2)\right)|X_1| + \\ &\quad r_1 L_{s0}^{-1}(|U| + |E|) + \left(r_1 L_{s0}^{-1} + 1\right)l \\ &= \Theta^{\mathrm{T}}\sigma + \varsigma \end{aligned} \tag{6}$$

where $\Theta = \begin{bmatrix} (r_2 + r_1 L_{s0}^{-1}(R_0 + r_2)) \\ r_1 L_{s0}^{-1} \end{bmatrix}$, $\sigma = \begin{bmatrix} |X_1| \\ |U| + |E| \end{bmatrix}$, and $\varsigma = (r_1 {L_{s0}}^{-1} + 1)l$.

Remake 1: From (6), we can obtain the boundary of unmodeled disturbance, which can help to construct the sliding mode gain and guarantee the stability of the control system.

III. Baseline Observer Design and Analysis

A. Traditional SMO Design

To design the observer, the following auxiliary dynamics are introduced from (5):

$$X_1 = \frac{1}{L_{s0}}(-R_0 X_1 + U + F) \tag{7}$$

where $F = \begin{bmatrix} F_\alpha & F_\beta \end{bmatrix}^{\mathrm{T}} = \begin{bmatrix} E_\alpha + \delta_\alpha & E_\beta + \delta_\beta \end{bmatrix}^{\mathrm{T}}$, F is bounded by $\max\{|e_\alpha| + l, |e_\beta| + l\}$, denote $\hat{X}_1 = \begin{bmatrix} \hat{i}_\alpha & \hat{i}_\beta \end{bmatrix}^{\mathrm{T}}$, the traditional SMO can be configured as follows to get an estimate of the extended BEF:

$$\dot{\hat{X}}_1 = \frac{1}{L_{s0}}\left(-R_0 \hat{X}_1 + U + Z_1\right) \tag{8}$$

where $Z_1 = K\,\mathrm{sgn}(X_1)$, subtract (5) from (7) yields

$$\dot{\tilde{X}}_1 = \frac{1}{L_{s0}}\left(-R_0 \tilde{X}_1 + Z_1 - F\right) \tag{9}$$

where $\tilde{X}_1 = \hat{X}_1 - X_1$, $\tilde{X}_1$ is the observer error of the current.

B. Stability Analysis of Traditional SMO

The result for the SMO is summarized in the following theorem, and stability analysis is provided.

Theorem 1: Consider the dynamic equation of PMIWM with disturbance error; the estimated current can converge in finite time under traditional SMO.

Proof: Select the following Lyapunov function V_1 as:

$$V_1 = \frac{1}{2}\dot{\tilde{X}}_1^{\,2}. \tag{10}$$

Differentiate (10) with respect to time and using (9), the following result could be established:

$$\begin{aligned} \dot{V}_1 &= \tilde{X}_1^{\mathrm{T}}\dot{\tilde{X}}_1 \\ &= \tilde{X}_1^{\mathrm{T}}\left[\left[\frac{1}{L_{s0}}\left(-R_0\tilde{X}_1 + Z_1 - F\right)\right]\right] \\ &= \tilde{X}_1^{\mathrm{T}} \cdot \left[\frac{1}{L_{s0}}\left(-R_0\tilde{X}_1 - F - K\,\mathrm{sgn}\left(\tilde{X}_1\right)\right)\right] \\ &= -\frac{R_0}{L_{s0}}\tilde{X}_1^{\mathrm{T}}\tilde{X}_1 - \frac{K}{L_{s0}}\left|\tilde{X}_1^{\mathrm{T}}\right| - \frac{F}{L_{s0}}\tilde{X}_1^{\mathrm{T}}. \end{aligned} \tag{11}$$

When sliding mode gain K meets $K \ge (|E| + |\delta|)/L_{s0}$, From (6), we denote $K = (\Theta^{\mathrm{T}}\sigma + \varsigma + f(t))/L$, $f(t) = \max(e_\alpha, e_\beta)$, the estimation error under the adaptive disturbance observer in (9) will converge to a bounded region in finite time.

This completes the proof of Theorem 1.

When traditional SMO enters sliding mode, $\tilde{X}_1 = \dot{\tilde{X}}_1 = 0$, we can obtain an estimation of the PMIWM's BEF from (6) as

$$\begin{bmatrix} F_\alpha \\ F_\beta \end{bmatrix} = \begin{bmatrix} e_\alpha \\ e_\beta \end{bmatrix} + \begin{bmatrix} \delta_\alpha \\ \delta_\beta \end{bmatrix} = K\begin{bmatrix} \mathrm{sgn}\left(i - \hat{i}_\alpha\right) \\ \mathrm{sgn}\left(i - \hat{i}_\beta\right) \end{bmatrix}. \tag{12}$$

Equation (12) shows the conventional SMO-based BEF estimation result. In order to improve the control of the estimation accuracy, we need to obtain the estimation value of the δ_α and δ_β, because the frequency of unmodeled disturbances in the

motor is much lower than that of the BEF, the BEF can be obtained by high-pass filtering of F, there is

$$\begin{bmatrix} e_\alpha \\ e_\beta \end{bmatrix} = \frac{s}{s + w_c} \begin{bmatrix} F_\alpha \\ F_\beta \end{bmatrix}. \tag{13}$$

Remake 2: Equation (13) inherently contains high-frequency sign function switching components. Arctangent-function-driven rotor position extraction techniques amplify these discontinuous signals, inducing persistent chattering values in electromechanical systems [28].

IV. Super-Twisting SMO

A. STSMO Design

This section implements an STSMO within a second-order sliding mode control framework to mitigate persistent high-frequency oscillations inherent in conventional SMO. Integrating a continuous switching function into the observer architecture makes the model trajectory smooth and continuous, reducing the system's chattering value. Design the STSMO as follows:

$$\dot{\hat{X}}_1 = \frac{1}{L_{s0}}\left(-R_0 \hat{X}_1 + U + V\right) \tag{14}$$

$$V = \begin{bmatrix} V_\alpha \\ V_\beta \end{bmatrix} = \begin{bmatrix} k_{\alpha,1}\left|\tilde{i}_\alpha\right|^{1/2} \operatorname{sgn}\left(\tilde{i}_\alpha\right) + \zeta_\alpha \\ k_{\beta,1}\left|\tilde{i}_\beta\right|^{1/2} \operatorname{sgn}\left(\tilde{i}_\beta\right) + \zeta_\beta \end{bmatrix} \tag{15}$$

$$\begin{bmatrix} \dot{\zeta}_\alpha \\ \dot{\zeta}_\beta \end{bmatrix} = \begin{bmatrix} -k_{\alpha,2} \operatorname{sgn}\left(\tilde{i}_\alpha\right) \\ -k_{\beta,2} \operatorname{sgn}\left(\tilde{i}_\beta\right) \end{bmatrix} \tag{16}$$

where V_α and V_β are the observed value of F. Subtract (7) from (14) and the current error can be obtained as follows:

$$\frac{d}{dt}\begin{bmatrix} \tilde{i}_\alpha \\ \tilde{i}_\beta \end{bmatrix} = -\frac{R_0}{L_{s0}}\begin{bmatrix} \tilde{i}_\alpha \\ \tilde{i}_\beta \end{bmatrix} + \frac{1}{L_s}\left|\begin{bmatrix} V_\alpha \\ V_\beta \end{bmatrix} - \frac{1}{L_{s0}}\begin{bmatrix} F_\alpha \\ F_\beta \end{bmatrix}\right. . \tag{17}$$

Design the sliding mode surface as

$$s^{\mathrm{T}} = \begin{bmatrix} \tilde{i}_\alpha & \tilde{i}_\beta \end{bmatrix}. \tag{18}$$

Combine (16) and (14), we can obtain current error equation as follows:

$$\frac{d}{dt}\begin{bmatrix} \tilde{i}_\alpha \\ \tilde{i}_\beta \end{bmatrix} = \begin{bmatrix} k_{\alpha,1}\left|\tilde{i}_\alpha\right|^{1/2} \operatorname{sign}\left(\tilde{i}_\alpha\right) \\ k_{\beta,1}\left|\tilde{i}_\beta\right|^{1/2} \operatorname{sign}\left(\tilde{i}_\beta\right) \end{bmatrix} + \begin{bmatrix} \zeta_\alpha \\ \zeta_\beta \end{bmatrix} - \begin{bmatrix} T_1 \\ T_2 \end{bmatrix} \tag{19}$$

where

$$\begin{cases} T_1 = -\dfrac{R_0}{L_{s0}}\tilde{i}_\alpha - \dfrac{1}{L_{s0}}F_\alpha \\ T_2 = -\dfrac{R_0}{L_{s0}}\tilde{i}_\beta - \dfrac{1}{L_{s0}}F_\beta. \end{cases} \tag{20}$$

Denote T_1 and T_2 are bounded with

$$\begin{cases} |T_1| \le \delta_1\left|\tilde{i}_\alpha\right|^{1/2} \\ |T_2| \le \delta_2\left|\tilde{i}_\beta\right|^{1/2}. \end{cases} \tag{21}$$

Hence, the sliding mode occurs when $s = \dot{s} = 0$, that means $\begin{bmatrix} \tilde{i}_\alpha \\ \tilde{i}_\beta \end{bmatrix} = \begin{bmatrix} \dot{\tilde{i}}_\alpha \\ \dot{\tilde{i}}_\beta \end{bmatrix} = 0$. We can obtain an estimation of the PMIWM's BEF as

$$F = \begin{bmatrix} e_\alpha \\ e_\beta \end{bmatrix} + \begin{bmatrix} \delta_\alpha \\ \delta_\beta \end{bmatrix} = \begin{bmatrix} V_\alpha \\ V_\beta \end{bmatrix}$$

$$= \begin{bmatrix} k_{\alpha,1}\left|\tilde{i}_\alpha\right|^{1/2} \operatorname{sign}\left(\tilde{i}_\alpha\right) + \varsigma_{\alpha,1} \\ k_{\beta,1}\left|\tilde{i}_\beta\right|^{1/2} \operatorname{sign}\left(\tilde{i}_\beta\right) + \varsigma_{\beta,1} \end{bmatrix}. \tag{22}$$

The BEF can be obtained by high-pass filtering of F, as shown in (13).

B. Stability Analysis of Traditional STSMO

The result for the proposed controller is summarized in the following theorem, and stability analysis is provided.

Theorem 2: Consider the dynamic equation of PMIWM with disturbance error, the estimated current can converge in finite time under STSMO

Proof: Because the alpha and beta axes are symmetrical to each other, we use the alpha axis as an example to demonstrate stability. This proof can be decomposed into the following three steps.

Step 1: Substitute the observation error into the motor model and observer model

$$\begin{aligned} \frac{d\tilde{i}_\alpha}{dt} &= \frac{di_\alpha}{dt} - \frac{d\hat{i}_\alpha}{dt} \\ &= \frac{1}{L_{s_0}}(u_\alpha - R_0 i_\alpha - F_\alpha) - \frac{1}{L_{s_0}}\left(u_\alpha - R_0\hat{i}_\alpha - V_\alpha\right) \\ &= -\frac{R_0}{L_{s_0}}\left(i_\alpha - \hat{i}_\alpha\right) + \frac{1}{L_{s_0}}(V_\alpha - F_\alpha) \\ &= -\frac{R_0}{L_{s_0}}\tilde{i}_\alpha + \frac{1}{L_{s_0}}(V_\alpha - F_\alpha). \end{aligned} \tag{23}$$

Substitute (15) into (23), we can obtain

$$\frac{d\tilde{i}_\alpha}{dt} = -\frac{R_0}{L_{s0}}\tilde{i}_\alpha - \frac{k_{\alpha,1}}{L_{s0}}\left|\tilde{i}_\alpha\right|^{1/2} \operatorname{sign}\left(\tilde{i}_\alpha\right) + \frac{1}{L_{s0}}(\zeta_\alpha - F_\alpha). \tag{24}$$

Step 2: Define new state variables to construct the Lyapunov equation.

Define new auxiliary variables as follows [29]:

$$\begin{cases} z_1 = \tilde{i}_\alpha \\ z_2 = \zeta_\alpha - F_\alpha. \end{cases} \tag{25}$$

Campared with ζ_α, F_α changes more slowly, so we denote $(dF_\alpha)/(dt) \approx 0$. Take the derivative of (25) with respect to time, we obtain

$$\begin{cases} \dfrac{dz_1}{dt} = \dfrac{d\tilde{i}_\alpha}{dt} = -\dfrac{R_0}{L_{s0}}z_1 - \dfrac{k_{\alpha,1}}{L_s}|z_1|^{1/2} \operatorname{sign}(z_1) + \dfrac{1}{L_s}z_2 \\ \dfrac{dz_2}{dt} = \dfrac{d\zeta_\alpha}{dt} - \dfrac{dF_\alpha}{dt} = \dfrac{d\zeta_\alpha}{dt} = -k_{\alpha,2} \operatorname{sign}\left(\tilde{i}_\alpha\right). \end{cases} \tag{26}$$

Step 3: Choose the Lyapunov function to validate the stability.

Choose a positive definite function as follows:

$$V_2 = \xi^{\mathrm{T}} P \xi = [\xi_1, \xi_2] P \begin{bmatrix} \xi_1 \\ \xi_2 \end{bmatrix} \tag{27}$$

where $\xi_1 = |x_1|^{1/2} \operatorname{sign}(x_1)$, $\xi_2 = z$, $P = 1/2\begin{bmatrix} 4\,k_{a,2} + k_{a,1}^2 & -k_{a,1} \\ -k_{a,1} & 2 \end{bmatrix}$.

Differentiate (27) with respect to time, and the following result could be established:

$$\frac{dV_2}{dt} = \frac{1}{|\xi_1|}\xi^{\mathrm{T}}\left(A^{\mathrm{T}}P + \mathrm{PA}\right)\xi \tag{28}$$

$$A = \begin{bmatrix} -\frac{R_s}{2L_{s0}}|\xi_1| - \frac{k_{\alpha,1}}{2L_{s0}} & \frac{1}{2L_{s0}} \\ -k_{\alpha,2}|\xi_1| & 0 \end{bmatrix}. \tag{29}$$

If there exists a positive definite matrix Q, which meets

$$A^{\mathrm{T}}P + \mathrm{PA} = -Q. \tag{30}$$

There is

$$\frac{dV_2}{dt} = -\frac{1}{|\xi_1|}\xi^{\mathrm{T}}Q\xi < 0. \tag{31}$$

In order to meet (30), the sliding mode control parameters satisfy

$$\begin{cases} k_{\alpha,1} > 0 \\ k_{\alpha,2} > 0 \\ k_{\alpha,2} > \dfrac{k_{\alpha,1}^2}{4} \cdot \dfrac{k_{\alpha,1}L_{s0} - \Gamma}{k_{\alpha,1}L_{s0} + \Gamma} \end{cases} \tag{32}$$

where Γ is the bound of the F_α. This completes the proof of Theorem 2.

C. Comparison of the BEF Obtained From Traditional the SMO and STSMO

From (12) and (22), the BEF of the traditional SMO and STSMO can be obtained, respectively. We take the BEF e_α as the research to analyze the chattering phenomenon, which can be obtained from the traditional SMO as

$$e_\alpha = \frac{s}{s+w}\left[K\,\mathrm{sgn}\left(\tilde{i}_\alpha\right)\right]. \tag{33}$$

The usual SMO yielded $\mathrm{sgn}(\tilde{i}_\alpha)$ as the discontinuous term of e_α. As the sliding mode surface s gets closer to zero, there is

$$\lim_{\tilde{i}_\alpha \to 0^-} K\mathrm{sgn}\left(\tilde{i}_\alpha\right) = -K \neq \lim_{\tilde{i}_\alpha \to 0^+} K\mathrm{sgn}\left(\tilde{i}_\alpha\right) = K. \tag{34}$$

From (34), we can conclude that e_α will experience a severe chattering phenomenon near the zero point, which can influence the estimation precision of the BEF. The BEF e_α obtained from the STSMO can be obtained from (13) as

$$e_\alpha = \frac{s}{s+w_c}\left[k_{\alpha,1}\left|\tilde{i}_\alpha\right|^{1/2}\mathrm{sgn}\left(\tilde{i}_\alpha\right) + \varsigma_{\alpha,1}\right]. \tag{35}$$

From (34), the chattering phenomenon caused by discontinuous term $\mathrm{sgn}(\tilde{i}_\alpha)$ is included in homogeneous function part $k_{\alpha,1}|\tilde{i}_\alpha|^{1/2}\mathrm{sgn}(\tilde{i}_\alpha)$ and integral function part $k_{\alpha,2}\int \mathrm{sgn}(\tilde{i}_\alpha)d\tau$, the above function graph is shown in Fig. 2.

As for the homogeneous function part $k_{\alpha,1}|\tilde{i}_\alpha|^{1/2}\mathrm{sgn}(\tilde{i}_\alpha)$, which can make discontinuous part $\mathrm{sgn}(\tilde{i}_\alpha)$ continuous. When the sliding mode surface S approaches the zero point, there is

$$\lim_{\tilde{i}_\alpha \to 0^-} k_{\alpha,1}\left|\tilde{i}_\alpha\right|^{\frac{1}{2}}\mathrm{sgn}\left(\tilde{i}_\alpha\right) = \lim_{\tilde{i}_\alpha \to 0^+} k_{\alpha,1}\left|\tilde{i}_\alpha\right|^{\frac{1}{2}}\mathrm{sgn}\left(\tilde{i}_\alpha\right) = 0. \tag{36}$$

In addition to making discontinuous parts continuous, the integral function part $k_{\alpha,2}\int \mathrm{sgn}(\tilde{i}_\alpha)d\tau$ can also lessen chattering when the sliding mode surface hits the zero point

$$\lim_{\tilde{i}_\alpha \to 0^-} \int \mathrm{sgn}\left(\tilde{i}_\alpha\right)d\tau = \lim_{\tilde{i}_\alpha \to 0^+} \int \mathrm{sgn}\left(\tilde{i}_\alpha\right)d\tau = 0. \tag{37}$$

From (36) and (37), it can be concluded that STSMO can lessen the chattering phenomena as the sliding mode surface gets closer to the stable point, which effectively increases the BEF's estimation precision.

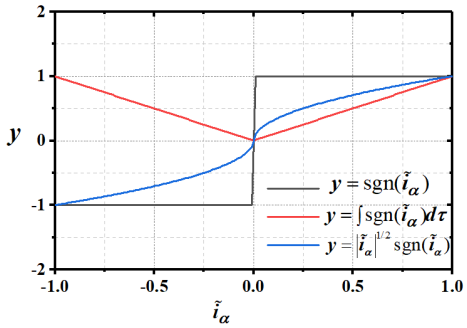

Fig. 2. Comparison of the functions.

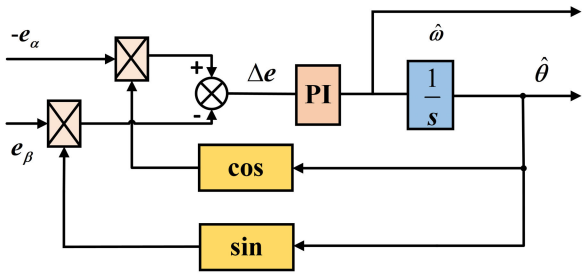

Fig. 3. Estimation of PLL.

D. Rotor Position Estimation Based on PLL

From the comparison of the BEF obtained from traditional the SMO and STSMO, we can conclude that STSMO can observe the position signal from BEF [30]:

$$\hat{\theta} = -\arctan\frac{e_\alpha}{e_\beta} = -\arctan\frac{U_\alpha}{U_\beta}. \tag{38}$$

As demonstrated in the preceding analysis, the proposed STSMO effectively mitigates chattering phenomena induced by discontinuous terms. However, the presence of switching functions $\mathrm{sgn}(\tilde{i}_\alpha)$ and $\mathrm{sgn}(\tilde{i}_\beta)$ in e_α and e_β introduces high-frequency oscillations [31]. These oscillations compromise the accuracy of the estimation process, leading to significant deviations in the derived outputs. A phase-locked loop (PLL) solves this issue by suppressing the high-frequency noise and enhancing estimation precision. The schematic of the proposed velocity and position estimation framework is illustrated in Fig. 3.

The subsequent equation can be derived from Fig. 3.

Denote $|e| = (e_\alpha{}^2 + e_\beta{}^2)^{1/2}$, then e_α and e_β can be expressed as

$$\Delta e = -e_\alpha\cos\hat{\theta} - e_\beta\sin\hat{\theta}. \tag{39}$$

Convert the stationary coordinate system components to polar coordinates

$$\begin{cases} e_\alpha = |e|\sin\theta \\ e_\beta = -|e|\cos\theta \end{cases} \tag{40}$$

substitute (39) into (40)

$$\begin{aligned} \Delta e &= -|e|\sin\theta\cos\theta + |e|\cos\theta\sin\theta \\ &= |e|\left(-\sin\theta\cos\hat{\theta} + \cos\theta\sin\hat{\theta}\right) \end{aligned}$$

$$= |e| \sin\left(\hat{\theta} - \theta\right)$$
$$= |e| \sin\left(\tilde{\theta}\right) \tag{41}$$

where $\tilde{\theta}$ denotes the deviation between $\hat{\theta}$ and θ, and $\tilde{\theta} = \hat{\theta} - \theta$. Equation (41) can be reduced as follows, when $|\tilde{\theta}| = |\hat{\theta} - \theta| \leq \pi/6$ is satisfied:

$$\Delta e = |e| \sin \tilde{\theta} \approx |e| \tilde{\theta}. \tag{42}$$

The PI controller's input signal Δe in Fig. 3 exhibits linear correlation with the rotor position estimation error $\tilde{\theta}$. Furthermore, the integral operation inherent to the PI structure inherently filters high-frequency switching components within Δe, generating smoothed outputs that stabilize the estimation loop.

Based on the aforementioned techniques, the following sequential steps are used to implement the suggested estimation methodology.

Step 1: Acquire the PMIWM stator currents and compute current estimation errors.

Step 2: Synthesize the FSTSMO using the current estimation errors and reconstruct BEF signals.

Step 3: Derive rotor position and speed estimates via the PLL-based method.

V. Control Parameters Analysis and Design of Fuzzy Controller

A. STSMO Control Parameters Analysis

Based on (35), we can obtain the BEF can be estimated by the STSMO, and the sliding mode control parameters of STSMO, such as $k_{\alpha,1}$, $k_{\alpha,2}$, $k_b,1$, and $k_b,2$ can affect the estimated precision of and further influence the control performance of the PMIWM, so that, we will discuss the discuss the relationship between control parameters and control speed, signal smoothness, and signal amplitude.

Regarding the speed of control, which is mainly determined by $k_{\alpha,2}$ and $k_b,2$, when these two parameters increase within an appropriate range, the convergence speed will increase accordingly.

As for the signal smoothness of BEF e_α, which will be influenced by both $k_{\alpha,1}$ and $k_{\alpha,2}$. When $k_{\alpha,2}$ increases, it can increase the control speed, but at the same time, it will lead to an increase in chattering and a decrease in smoothness.$k_{\alpha,1}$ mainly affects the convergence trajectory of the system near the sliding surface. Increasing $k_{\alpha,1}$ will suppress the chattering caused by $k_{\alpha,2}$ and improve the smoothness of the signal. However, excessive $k_{\alpha,1}$ may also lead to system overshoot or other instability phenomena.

In addition, signal amplitude is mainly influenced by $\varsigma_{\alpha,1}$ and $\varsigma_{\beta,1}$, their upper limit is directly determined by $k_{\alpha,2}$ and $k_b,2$, respectively. When these two parameters increase, the upper limit of $\varsigma_{\alpha,1}$ and $\varsigma_{\beta,1}$ will also increase, which can cause a bigger signal amplitude.

Remake 3: As given in (35), a key problem of STSMO is seeking the optimal balance between convergence speed, estimation smoothness, and robustness. In addition, due to the large number of parameters that need to be adjusted, it is easy to create a contradiction between approaching speed and chattering.

TABLE I
Corresponding Relation of Fuzzy Parameter $\Delta\lambda_1$

$\Delta\lambda_1$ (s \ $\dot{s}$)	NB	NM	ZO	PM	PB
NB	NB	NB	ZO	PB	PB
NM	NB	NM	ZO	PM	PB
ZO	NM	NM	ZO	PB	PB
PM	PM	PM	PM	PB	PB
PB	PM	PM	PM	PB	PB

B. Fuzzy Controller Design

The fixed nature of these four parameters k_a, 1, $ka,_2$, k_b, 1, and k_b, 2 throughout the control process fundamentally limits the system's ability to achieve both rapid convergence speed and minimal chattering magnitude simultaneously [31]. To resolve this, we develop an adaptive fuzzy controller that adjusts the sliding mode parameters to approach parameters through real-time fuzzy rule adaptation. This novel strategy enables an optimal equilibrium between chattering suppression and convergence acceleration. Furthermore, to streamline computational complexity in fuzzy controller implementation, we establish parameter coupling relationships through constraint conditions: $\Delta k_{\alpha,1} = \Delta k_b,_1 = \Delta\lambda_1$ and $\Delta k_{\alpha,2} = \Delta k_b,_2 = \Delta\lambda_2$. The fuzzy logic controller is synthesized through the following systematic procedure.

Step 1: Define the sliding mode surface variables s and $\dot{s}$ as the principal and auxiliary fuzzy inputs, respectively.

Step 2: Configure the controller's fuzzy outputs by designating the approaching rate parameters $\Delta\lambda_1$ and $\Delta\lambda_2$, creating a dual-output adjustment mechanism.

Step 3: Formulate the fuzzy rules and establish the fuzzy logic connecting the fuzzy inputs to the fuzzy outputs, resulting in 1–25 fuzzy rules as detailed below.

1) *R(1):* If s is A_1^1 and $\dot{s}$ is A_2^1, then $\Delta\lambda_1$ is B_1^1, and $\Delta\lambda_2$ is B_2^1.
2) *R(2):* If s is A_1^2 and $\dot{s}$ is A_2^1, then $\Delta\lambda_1$ is B_2^1, and $\Delta\lambda_2$ is B_2^2.
   ⋮
3) *R(25):* If s is A_1^5 and $\dot{s}$ is A_2^5, then $\Delta\lambda_1$ is B_2^{25}, and $\Delta\lambda_2$ is B_2^{25}.

The A_i^j is the fuzzy set of input. $i = 1, 2$, $j = 1, 2, \ldots\ldots, 5$, B_i^n is the fuzzy set of the conclusion, $i = 1, 2, n = 1, 2, \ldots\ldots, 25$, s and $\dot{s}$ are denoted as inputs for the fuzzy controller, $\Delta\lambda_1$ and $\Delta\lambda_2$ are assigned as control output for the fuzzy controller, with fuzzy rules designed in Tables I and II. Membership functions governing these parameters are illustrated in Fig. 4.

Remake 4: In traditional STSMO, although high gain $k_{\alpha,2}$ $k_b,_2$ can ensure fast convergence and strong robustness, it will introduce significant chattering. Although low gain can suppress chattering, it will reduce the dynamic response speed. The fuzzy STSMO can dynamically adjust the observer gain in real-time and nonlinearly based on the sliding mode s and its rate of change Δs by introducing fuzzy logic rules. When the error is large, the system automatically increases the

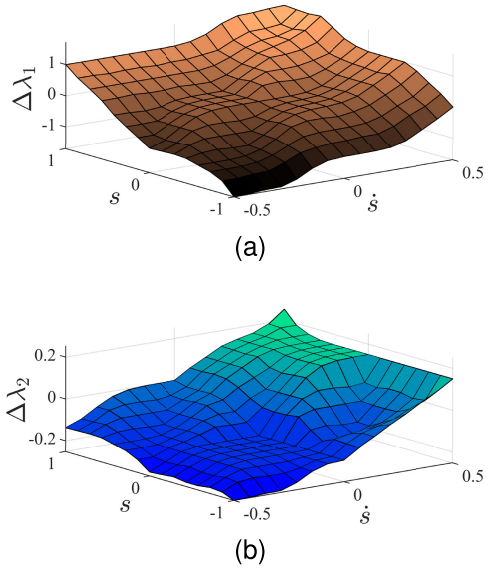

Fig. 4. Fuzzy relationship diagram (a) $\Delta\lambda_1$ and (b) $\Delta\lambda_2$.

TABLE II
CORRESPONDING RELATION OF FUZZY PARAMETER $\Delta\lambda_2$

$\Delta\lambda_2$ (s / $\dot{s}$)	NB	NM	ZO	PM	PB
NB	NB	NM	ZO	PM	PB
NM	NB	NM	NM	NM	ZO
ZO	NB	NM	ZO	ZO	ZO
PM	PM	PM	PM	PB	PM
PB	PB	PM	PB	PB	PB

gain to ensure fast convergence. When the error approaches zero, the intelligent system reduces the gain to suppress chattering and obtain a smoother estimation signal effectively. This adaptive-gain adjustment mechanism enables it to exhibit superior comprehensive performance under different operating conditions compared to traditional STSMO with fixed gain. It not only exhibits high robustness but also features a faster convergence speed and lower chattering level, significantly enhancing the practicality of the observer and the overall performance of the control system.

VI. SIMULATION AND EXPERIMENTS

This section describes the PMIWM sensorless drive system, as depicted in Fig. 5. The control architecture implements a two-tiered sliding mode strategy, incorporating velocity and current regulation loops, following the methodology as detailed in [32]. A unique aspect of this system is its hybrid sensing feature, which permits an effortless transition between conventional sensor-based control and sensorless estimation methods via a configuration switch. The sensorless observation subsystem functions alongside physical encoder measurements, with encoder data providing reference benchmarks to assess the accuracy of the sensorless estimations.

Comparative simulations are performed in MATLAB/Simulink to assess the suggested observer's efficacy. The simulations contrasted the suggested FSTSMO with the STSMO and the traditional SMO. The examination concentrated on essential performance metrics, encompassing the precision of angular position estimation, the efficacy of speed tracking, and the ability to reduce chattering.

A. Sensorless Control Simulation Test

This section outlines the simulation conducted in the PMIWM to assess the performance of FSTSMO, STSMO, and traditional SMO. The results for the state variable are illustrated in Fig. 6(a)–(d). The observed BEF values are illustrated in Fig. 7(a)–(c).

Fig. 6(a) illustrates the phase trajectory of the system state, commencing from its beginning point and employing three distinct sliding mode surfaces. The FSTSMO method exhibits a more rapid convergence than the STSMO and traditional SMO techniques. Fig. 6(b) depicts the convergence process of the system state utilizing these three sliding mode surfaces, indicating that FSTSMO attains a reduced steady-state error compared to the other observers. Fig. 6(c) highlights the control input u, indicating that FSTSMO generates more fluid control inputs with less chattering. Finally, Fig. 6(d) illustrates the position tracking trajectories for the two sliding mode surfaces, demonstrating that FSTSMO adheres to the reference position signal with greater speed and less inaccuracy. FSTSMO demonstrates enhanced performance relative to STSMO and traditional SMO regarding convergence velocity, minimization of steady-state error, and chattering mitigation.

Remake 5: The steady error occurred from the amplitude and phase errors contained in the estimated BEF, especially in low-speed regions. These errors will eventually be transmitted to the position and velocity estimation, resulting in a steady state. STSMO eliminates the chattering of traditional SMO by introducing a nonlinear term, which significantly reduces the phase lag problem, thereby enhancing its performance to surpass that of SMO. However, the stability and accuracy of STSMO still depend on the selection of its gain parameters. If the gain design is improper or if the system has unmodeled dynamic characteristics, it will still generate a small, finite steady-state error. This error is typically smaller than traditional SMO, but it is not easy to eliminate. Compared to the STSMO, the FSTSMO can adjust the sliding mode gain in real-time, optimizing the steady error.

Fig. 7 illustrates the outcomes of the simulated estimation tests for the BEF values e_α and e_β employing the FSTSMO, STSMO, and traditional SMO methodologies. Fig. 7(a) shows that the FSTSMO estimation strategy produces a smoother simulation curve and a lower total harmonic distortion (THD) when estimating the BEF values. The estimated fluctuations for e_α and e_β remain within 5 V. In contrast, the BEF estimation results using the STSMO and traditional SMO methods, as illustrated in Fig. 7(b) and (c), show more severe fluctuations and higher THD. These variations are primarily due to the chattering phenomenon inherent in these two observer methods.

Figs. 6 and 7 present a comparative analysis of the simulation tests conducted on state variables and BEF estimation within PMIWM using FSTSMO, STSMO, and conventional

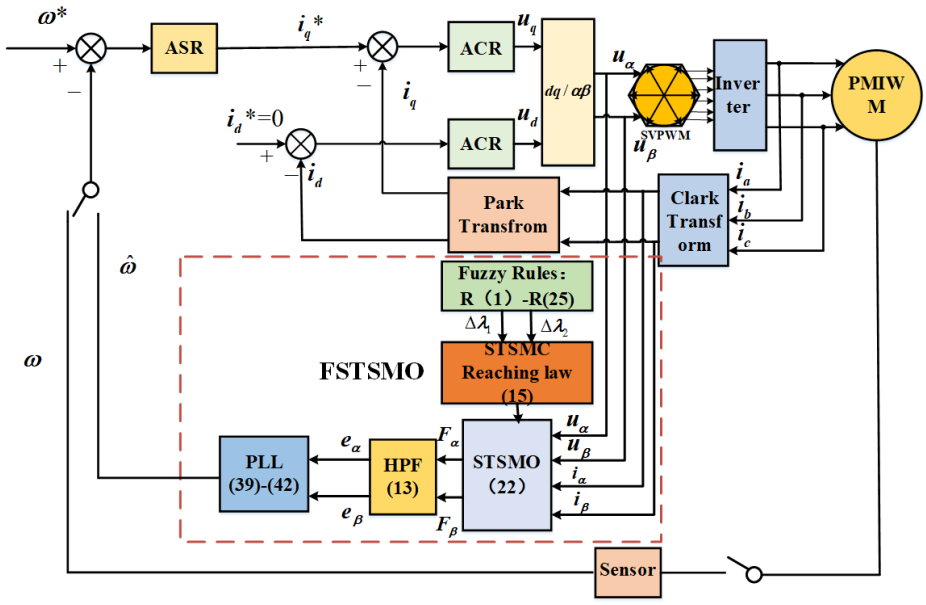

Fig. 5. PMIWM sensorless control system.

TABLE III
EVALUATION OF ESTIMATION PERFORMANCE OF OBSERVERS

Symbol	FSTSMO	STSMO	SMO
THD of e_α(%)	4.79	6.44	8.48
THD of e_β(%)	4.81	6.38	8.63
Maximum estimation fluctuation of e_α (V)	3.82	10.25	20.31
Maximum estimation fluctuation of e_β (V)	3.74	11.43	21.25

TABLE IV
MOTOR PARAMETERS

Symbol	parameter	Value
B	viscous friction coefficient	0.0065 N·m·s
L	d-axis and q-axis stator inductance	8.0 mH
J	moment of inertia	$0.004\text{kg}\cdot\text{m}^2$
ψ	Permanent magnet flux	0.385 Wb
R	Stator resistance	3.75 Ω
P	Pole pair number	4

TABLE V
PLATFORM COMPONENTS

Components	Name	Manufacturer/Location
Acquisition card	Links-IPC-DAQ-04	Links/China
PMIWM	PMIWM-01	Links/China
Load sensor	POB1KAO	Kilster/German
Control box	Links-Box-03	Links/China
Control software	RT-Sim Plu	Links/China

SMO approaches. The simulation results confirm that the proposed FSTSMO estimating technique markedly diminishes chattering in the control process via its optimal convergence rule (15), which can elinimate the chattering via by continuous and integral processing of the sign function $\text{sgn}(\tilde{i}_\alpha)$ and $\text{sgn}(\tilde{i}_\beta)$ leading to smoother waveform profiles and reduced fluctuation errors in the estimated values. These enhancements enable PMIWM to accurately predict position and velocity data during sensorless control operations, hence improving the overall control efficacy of PMIWM. Table III compares the estimation performance metrics across the different observers.

B. Sensorless Control Experimental Test

Expanding upon the prior sensorless control technique formulated in this article, employing FSTSMO, exhibits precise estimation capabilities for state variables and BEF. This section will outline the experimental evaluations conducted on the physical motor platform to verify the effectiveness of the proposed FSTSMO-PLL-based sensorless control method on the motor test platform. Fig. 8 illustrates the configuration of the motor platform and its control architecture.

The motor experimental testing platform has been created with the RT-Links simulation system. The assembly comprises a motor towing platform that contains a load motor, a torque sensor, and a driving motor. The configuration comprises an oscilloscope, a drive controller, and a personal computer. The motor specifications and the physical platform components are detailed in Tables IV and V, respectively.

To assess the efficacy of the FSTSMO-PLL-based sensorless control for PMIWM, we conduct tests of BEF, start-up, acceleration, loading, and position estimation. We then compare these experimental findings with those obtained using STSMO-PLL and conventional SMO-PLL methods.

Fig. 9 illustrates the experimental results of BEF employing the FSTSMO, STSMO, and traditional SMO methodologies. Fig. 9(a) presents that the FSTSMO method can estimate BEF with a smoother simulation curve and less fluctuation than the other two methods, which is mainly due to the continuity and integration of the sign function during the convergence process. The BEF estimation experimental results adopting STSMO and traditional SMO algorithms, as shown in Fig. 9(b) and (c), show greater fluctuations, which can cause a severe chattering phenomenon when further estimating the velocity and position signals.

Figs. 10 and 11 present the experimental results of low- and high-speed starting, conducted with a command of 200 and 1000 r/min, respectively, using three distinct SMO control

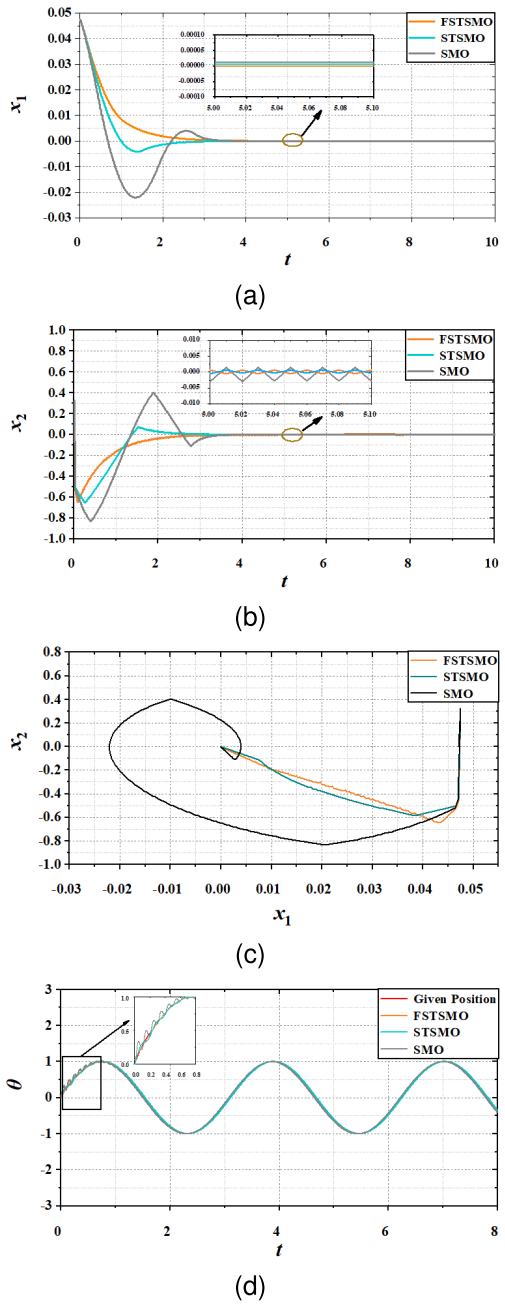

Fig. 6. Performance comparison between FSTSMO, STSMO, and SMO. (a) Phase trajectory. (b) Systemstate convergence. (c) Control input. (d) Position tracking.

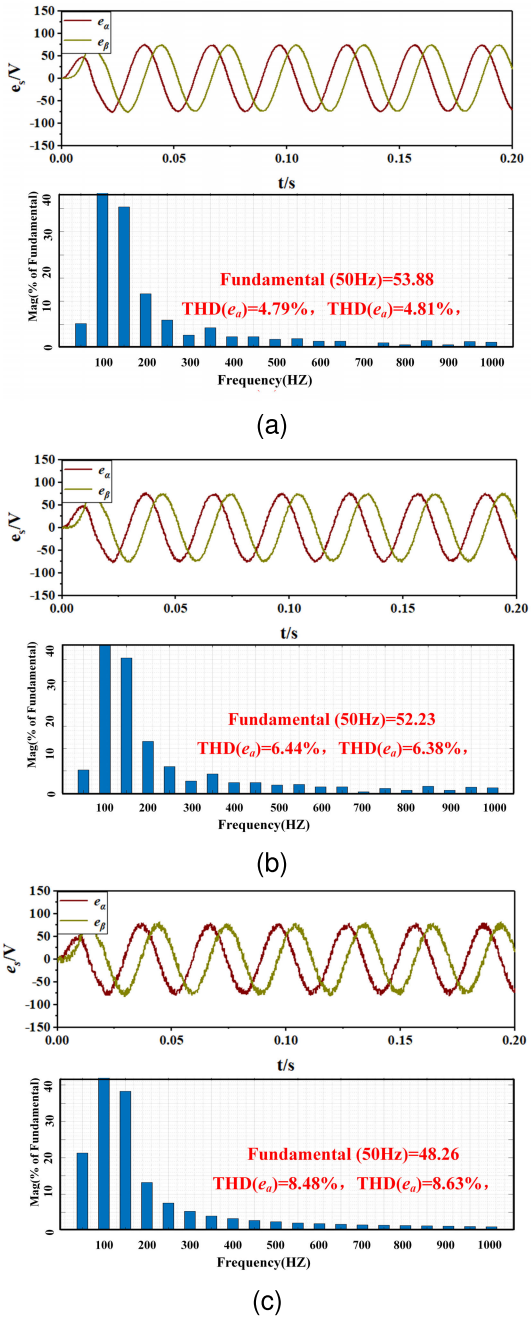

Fig. 7. Estimation simulation of e_s (a) FSTSMO, (b) STSMO, and (c) SMO.

algorithms: FSTSMO-PLL, STSMO-PLL, and SMO-PLL. Figs. 10(a) and 11(a) illustrate that the FSTSMO-PLL-based sensorless control can achieve a rapid start-up response and maintain a low tracking error during this phase. In contrast, the STSMO-PLL and SMO-PLL methods exhibit shortcomings in observation accuracy and position velocity extraction, leading to significant tracking errors at the beginning of their responses. Table VI presents a detailed comparison of starting performance.

We conducted low-to-medium-speed acceleration and high-speed experiments to evaluate the acceleration performance of the proposed sensorless control method. Figs. 12 and 13 illustrate the velocity observations and d-axis current results for PMIWM under three different control algorithms.

As depicted in Figs. 12 and 13, it can be observed that the FSTSMO-PLL control scheme facilitates acceleration without any overshoot, indicating superior performance compared to the other two control strategies. Furthermore, throughout the acceleration phase, the FSTSMO-PLL control scheme results in minimal fluctuations in the current i_d. Table VII presents a comprehensive comparison of acceleration performance.

The motor's physical configuration can be used to conduct loading and unloading experiments to assess the proposed sensorless control system's anti-disturbance efficacy. Fig. 14(a)–(c) shows the results of torque detection and velocity estimates for PMIWM under each control scheme.

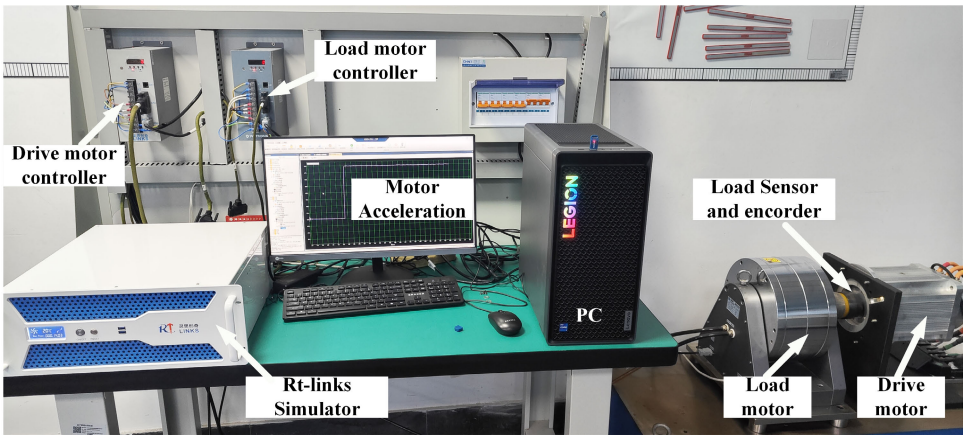

Fig. 8. Motor experimental testing platform.

TABLE VI
COMPARISON OF STARTING PERFORMANCE OF PMIWM

Symbol	SMO-PLL	STSMO-PLL	FSTSMO-PLL
low-speed starting tracking error (rpm)	75.2	118.6	173.4
low-speed stable tracking error (rpm)	0.9	2.3	3.6
high-speed starting tracking error (rpm)	213.5	254.7	263.3
high-speed stable tracking error (rpm)	5.5	7.2	9.8

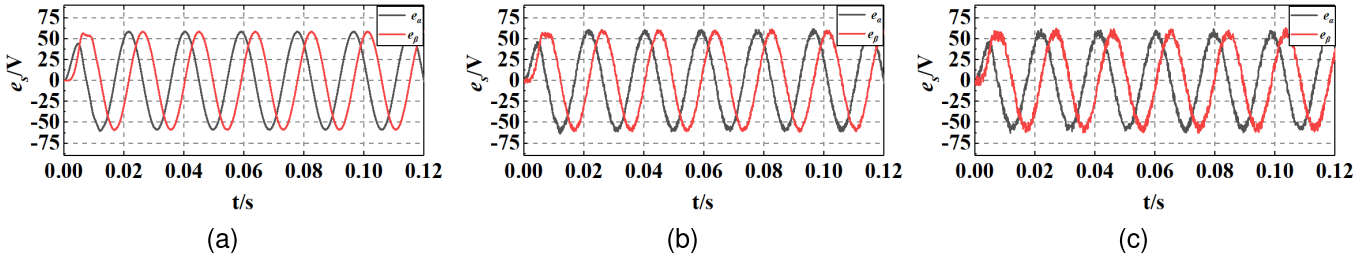

Fig. 9. Experimental test of BEF estimation (a) FSTSMO, (b) STSMO, and (c) SMO.

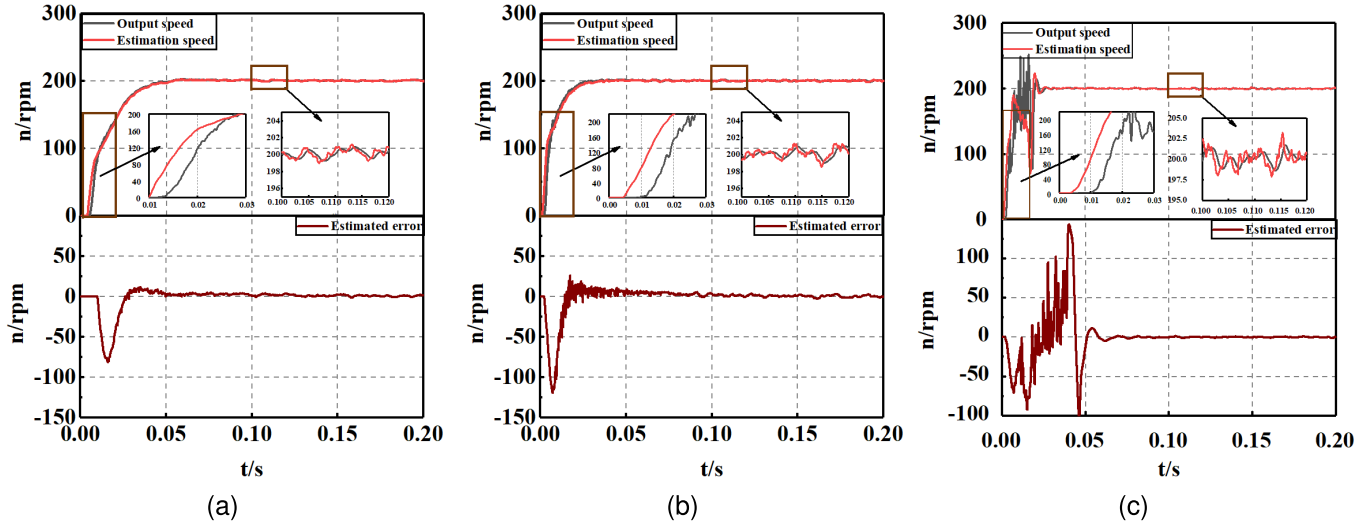

Fig. 10. Experimental test of low-speed starting (200 r/min) (a) FSTSMO-PLL, (b) STSMO-PLL, and (c) SMO-PLL.

As demonstrated in Fig. 14(a), the sensorless control strategy utilizing FSTSMO-PLL achieves exceptional speed regulation for the PMIWM, which can impressively maintain control within a tight range of 30 r/min even under challenging external load disturbances while ensuring the tracking error remains below 10 r/min during regulation. In contrast, the STSMO-PLL sensorless control system exhibits a significantly diminished ability to counteract interference, leading to output speed fluctuations that are more than four times greater than those seen with the

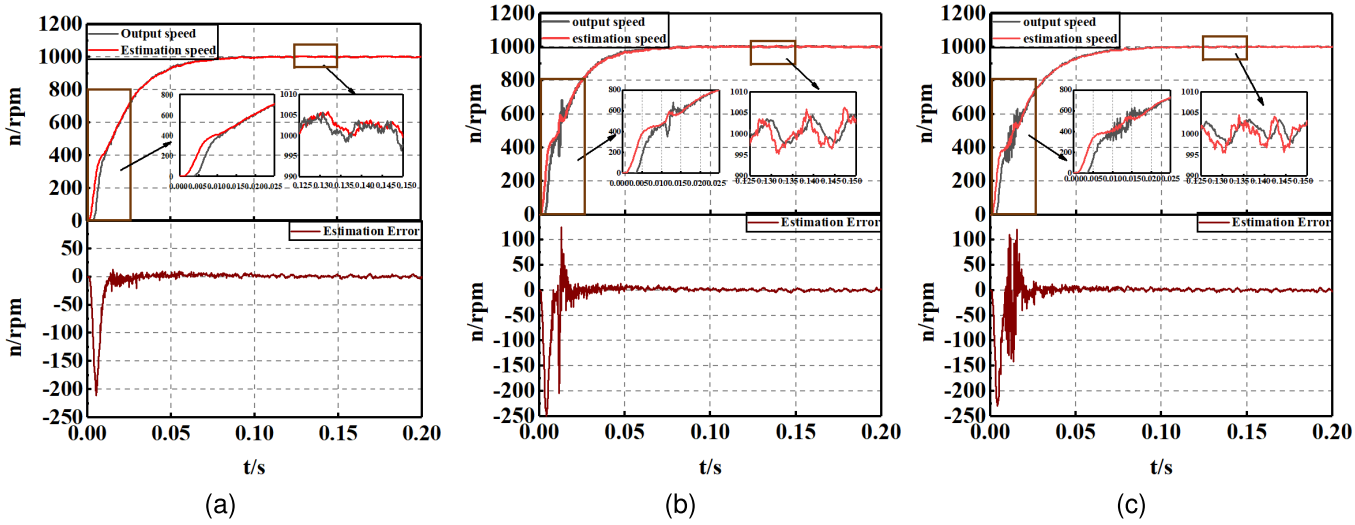

Fig. 11. Experimental test of high-speed starting (1000 r/min) (a) FSTSMO-PLL, (b) STSMO-PLL, and (c) SMO-PLL.

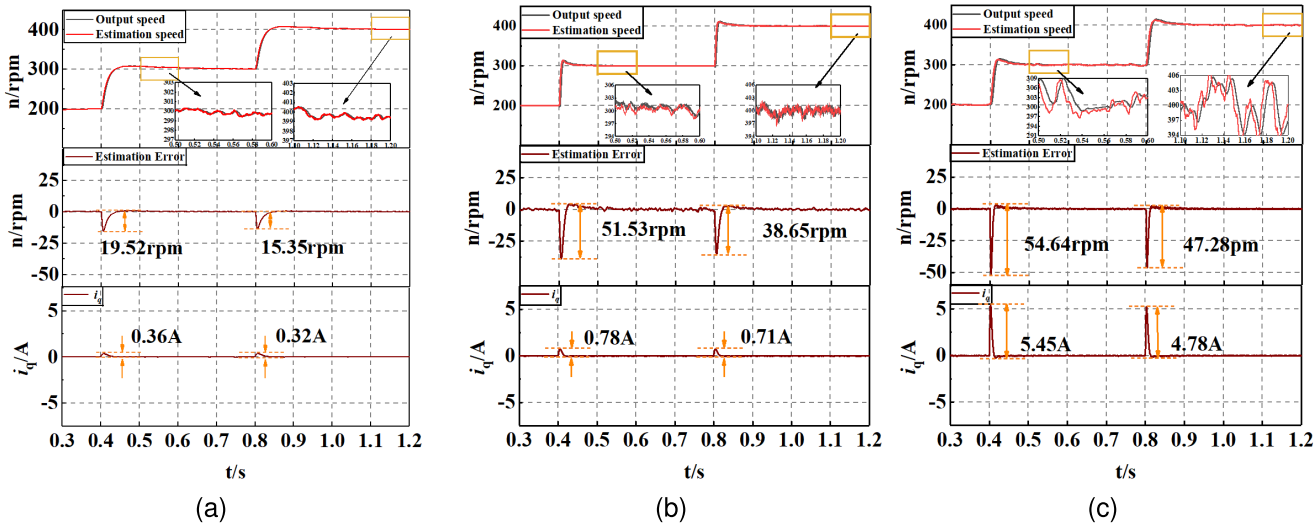

Fig. 12. Experimental test of low-to-medium-speed acceleration (a) FSTSMO-PLL, (b) STSMO-PLL, and (c) SMO-PLL.

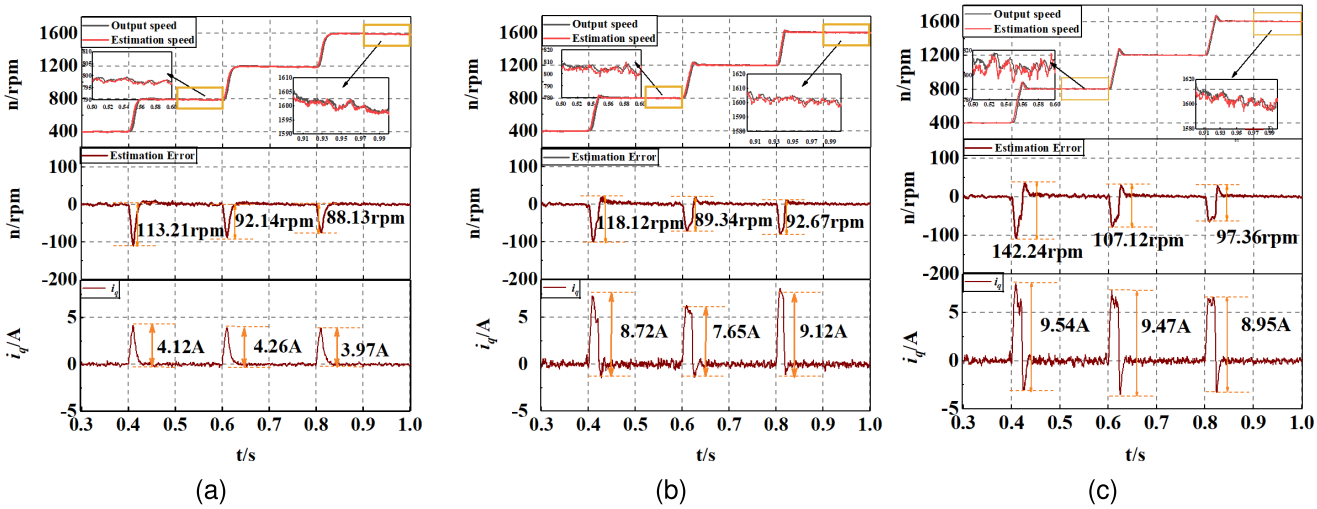

Fig. 13. Experimental test of medium-to-high-speed acceleration (a) FSTSMO-PLL, (b) STSMO-PLL, and (c) SMO-PLL.

FSTSMO-PLL method, as depicted in Fig. 14(b). Furthermore, the SMO-PLL sensorless control approach has significant amplitude variations and overshoots in output and observation values during load disturbances, with peak

TABLE VII
COMPARISON OF THE ACCELERATION PERFORMANCE OF PMIWM

Symbol	SMO-PLL	STSMO-PLL	FSTSMO-PLL
Mean acceleration response time (estimationd value) (s)	0.027	0.025	0.013
Mean acceleration response time (output value) (s)	0.028	0.024	0.012
Peak acceleration response overrun (r/min)	43.2	25.8	0
Peak acceleration current fluctuation (A)	18.24	17.46	12.53

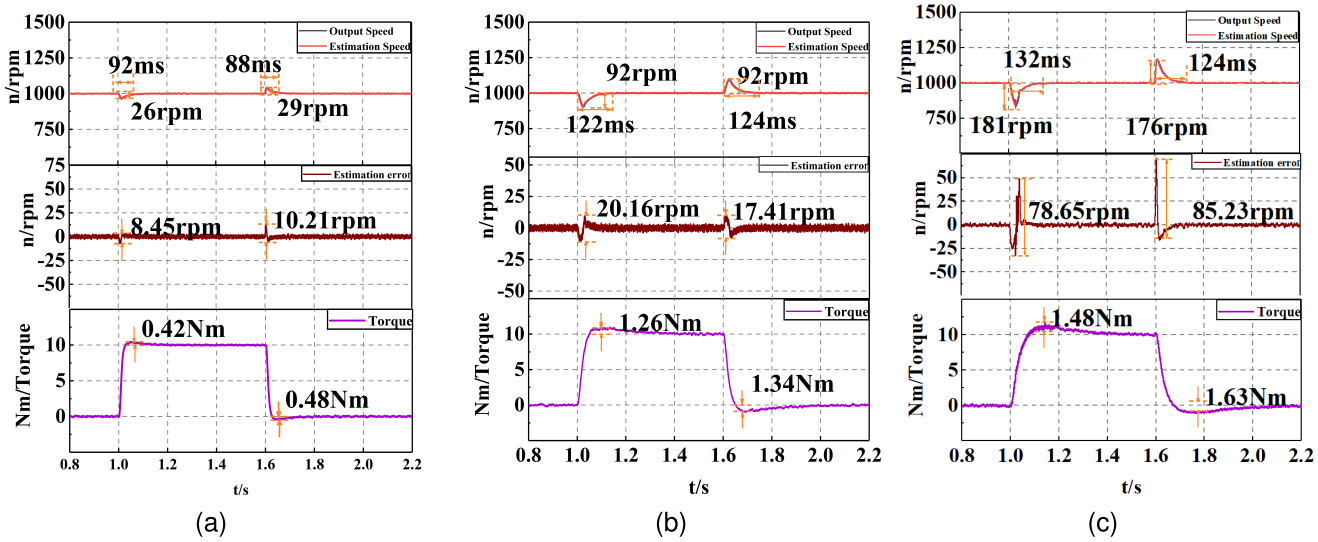

Fig. 14. Experimental test of loading (a) FSTSMO-PLL, (b) STSMO-PLL, and (c) SMO-PLL.

TABLE VIII
COMPARISON OF LOADING PERFORMANCE OF PMIWM

Symbol	SMO-PLL	STSMO-PLL	FSTSMO-PLL
Response time while loading (observed value) (s)	0.038	0.023	0.018
Response time while loading (output value) (s)	0.041	0.024	0.016
Response fluctuation while loading (observed value) (r/min)	94.2	48.5	32.7
Response fluctuation while loading (output value) (r/min)	93.8	47.3	32.3
Response time while unloading (observed value) (s)	0.042	0.030	0.013
Response time while unloading (output value) (s)	0.045	0.029	0.012
Response fluctuation while unloading (observed value) (r/min)	88.3	46.6	29.3
Response fluctuation while unloading (output value) (r/min)	87.6	45.3	28.5

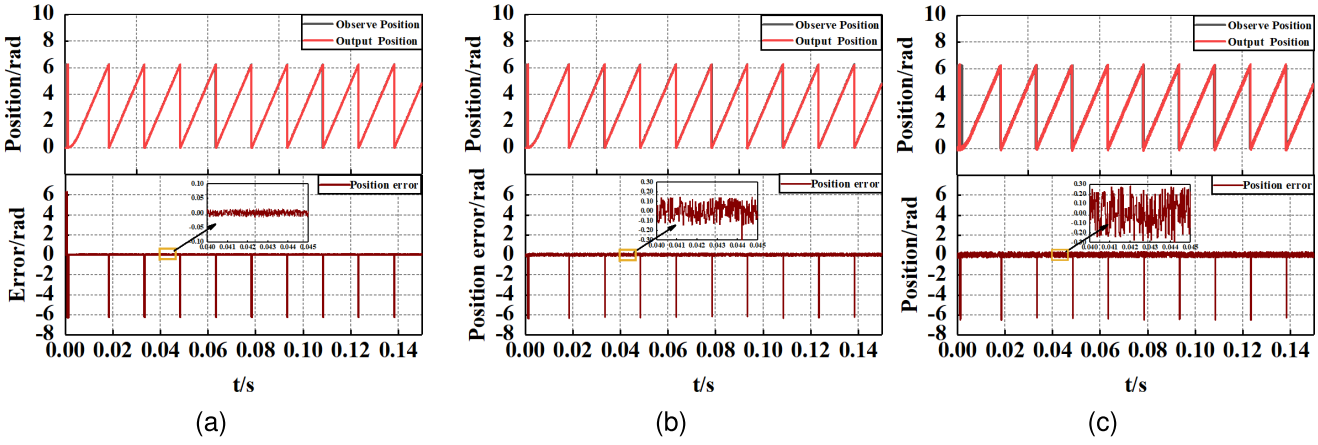

Fig. 15. Experimental test of position estimation (a) FSTSMO-PLL, (b) STSMO-PLL, and (c) SMO-PLL.

output fluctuations exceeding 181 r/min. These compelling experimental results highlight the ideal anti-interference and robustness of the FSTSMO-PLL sensorless control strategy. Even with large load fluctuations, the proposed FSTSMO-PLL sensorless technique ensures PMIWM performance stability. Table VIII presents a comprehensive comparison of loading performance.

Remark 6: It should be noted that the chattering as observed from the STSMO is slightly than the SMO, as shown in Figs. 9–14, which is main because STSMO can achieve

continuity and integration of the sign function $\text{sgn}(\tilde{i}_\alpha)$ and $\text{sgn}(\tilde{i}_\beta)$ during the convergence process. Compared with STSMO, the proposed FSTSMO can realize more ideal control performance, which is due to the real-time adjustment of sliding mode parameteres of STSMO through the fuzzy rules (1)–(25), the fuzzy controller can adjust control parameters $k_{\alpha,1}$, $k_{\alpha,2}$, $k_{b,1}$, and $k_{b,2}$ in (35) and achieve a balance of the chattering value and response speed of the control system.

The proposed FSTSMO-PLL-based position estimate methodology's performance is experimentally confirmed at 1000-r/min reference speed. The evaluation used a high-resolution 2500-line optical encoder to measure the rotor position precisely. Fig. 15 illustrates the suggested method's efficacy under various operating situations by providing a thorough comparison of position estimate accuracy for three distinct control systems.

Comparative analysis of experimental results in Fig. 15(a)–(c) reveals distinct performance characteristics among the three PMIWM rotor position estimation strategies. The proposed FSTSMO-PLL-based sensorless control strategy demonstrates superior performance with bounded tracking error maintained below 0.25 rad, indicating enhanced estimation accuracy and dynamic stability. In contrast, conventional STSMO-PLL implementation exhibits persistent oscillations with approximately 8% amplitude deviation in steady-state operation. At the same time, the SMO-PLL scheme shows significant estimation inaccuracies exceeding 0.4-rad tracking error accompanied by amplitude deviations surpassing 10%. These comparative metrics quantitatively confirm the effectiveness of the proposed adaptive-gain modulation mechanism in suppressing harmonic distortion and improving transient response characteristics.

VII. Conclusion

This study presents a novel FSTSMO integrated with PLL estimation for enhanced sensorless control of PMIWM systems. The proposed methodology addresses three critical technical challenges as follows.

1) An STSMO architecture was developed to eliminate position sensors while suppressing high-frequency chattering by 52.3% compared to conventional SMO implementations, as quantified by BEF harmonic analysis.
2) An adaptive fuzzy logic controller was designed to optimize STSMO gain parameters dynamically, achieving state variable convergence within 0.15 s.
3) A hybrid PLL estimation algorithm was implemented, reducing rotor position estimation error to 0.25 rad and improving disturbance rejection capability by 67%.

Our future work will pursue two main directions. First, we will implement the algorithm on FPGA hardware to achieve accelerated real-time control performance. Second, we will explore neural network-assisted gain scheduling. While the current fuzzy logic controller provides a transparent and effective baseline, its performance is inherently constrained by the pre-defined expert knowledge. Neural networks are envisioned as a means to learn more complex, high-dimensional gain scheduling policies directly from operational data, thereby overcoming this limitation and further enhancing the system's transient performance and adaptability to unmodeled dynamics.

Declaration of Competing Interest

The authors declare that they have no known competing financial interests or personal relationships that could have appeared to influence the work reported in this article.

References

[1] S. Zhang, A. Shen, X. Luo, Q. Tang, and Z. Li, "Multi-sliding mode current disturbance suppression scheme based model reference adaptive system for sensorless control of permanent magnet synchronous motor," *ISA Trans.*, vol. 137, pp. 615–628, Jun. 2023.

[2] C. Liu, H. Liu, L. Han, W. Wang, and C. Guo, "Multi-level coordinated yaw stability control based on sliding mode predictive control for distributed drive electric vehicles under extreme conditions," *IEEE Trans. Veh. Technol.*, vol. 72, no. 1, pp. 280–296, Jan. 2023.

[3] R. Lacombe, S. Gros, N. Murgovski, and B. Kulcsár, "Distributed eco-driving control of a platoon of electric vehicles through Riccati recursion," *IEEE Trans. Intell. Transp. Syst.*, vol. 24, no. 3, pp. 3048–3063, Mar. 2023.

[4] Z. Chen, R. Xiong, X. Cai, Z. Wang, and R. Yang, "Regenerative braking control strategy for distributed drive electric vehicles based on slope and mass co-estimation," *IEEE Trans. Intell. Transp. Syst.*, vol. 24, no. 12, pp. 14610–14619, Dec. 2023.

[5] K. Yu and Z. Wang, "Position sensorless control of IPMSM using adjustable frequency setting square-wave voltage injection," *IEEE Trans. Power Electron.*, vol. 37, no. 11, pp. 12973–12979, Nov. 2022.

[6] Z. Feng, S. Zhao, W. Gao, Y. Zhang, and L. Fei, "Study on a novel in-wheel motor driving system driven by two permanent magnet synchronous disc motors," *IEEE Trans. Veh. Technol.*, vol. 72, no. 5, pp. 5922–5933, May 2023.

[7] X. Kong, Y. Hua, Z. Zhang, C. Wang, and Y. Liu, "Analytical modeling of high-torque-density spoke-type permanent magnet in-wheel motor accounting for rotor slot and eccentric magnetic pole," *IEEE Trans. Transport. Electrific.*, vol. 7, no. 4, pp. 2683–2693, Dec. 2021.

[8] K. Zhao et al., "Robust model-free super-twisting sliding-mode control method based on extended sliding-mode disturbance observer for PMSM drive system," *Control Eng. Pract.*, vol. 139, Oct. 2023, Art. no. 105657.

[9] W. Chen, J. Gao, and C. Gao, "Disturbance observer-based saturated optimal super-twisting integral sliding mode midcourse guidance against maneuvering targets," *Control Eng. Pract.*, vol. 157, Apr. 2025, Art. no. 106242.

[10] X. Guo, S. Huang, K. Lu, Y. Peng, H. Wang, and J. Yang, "A fast sliding mode speed controller for PMSM based on new compound reaching law with improved sliding mode observer," *IEEE Trans. Transport. Electrific.*, vol. 9, no. 2, pp. 2955–2968, Jun. 2023.

[11] Y. Mi, Y. Song, Y. Fu, and C. Wang, "The adaptive sliding mode reactive power control strategy for wind–diesel power system based on sliding mode observer," *IEEE Trans. Sustain. Energy*, vol. 11, no. 4, pp. 2241–2251, Oct. 2020.

[12] Y. Wang, Y. Zhu, X. Zhang, B. Tian, K. Wang, and J. Liang, "Antidisturbance sliding mode-based deadbeat direct torque control for PMSM speed regulation system," *IEEE Trans. Transport. Electrific.*, vol. 7, no. 4, pp. 2705–2714, Dec. 2021.

[13] J. Kong and W. Zhang, "A new fast observer-based speed control algorithm for PMSM motor drive based on sliding mode theory," *Int. J. Dyn. Control*, vol. 12, no. 12, pp. 4274–4283, Dec. 2024.

[14] P. Zhang, Y. Kao, J. Hu, B. Niu, H. Xia, and C. Wang, "Finite-time observer-based sliding-mode control for Markovian jump systems with switching chain: Average dwell-time method," *IEEE Trans. Cybern.*, vol. 53, no. 1, pp. 248–261, Jan. 2023.

[15] B. Ding, D. Xu, B. Jiang, P. Shi, and W. Yang, "Disturbance-observer-based terminal sliding mode control for linear traction system with prescribed performance," *IEEE Trans. Transport. Electrific.*, vol. 7, no. 2, pp. 649–658, Jun. 2021.

[16] S. Wang et al., "Sensorless control strategy for permanent magnet synchronous motor based on adaptive non-singular fast terminal sliding mode observer," *IEEE Trans. Appl. Supercond.*, vol. 34, no. 8, pp. 1–5, Nov. 2024.

[17] K. Zhang, L. Wang, and X. Fang, "High-order fast nonsingular terminal sliding mode control of permanent magnet linear motor based on double disturbance observer," *IEEE Trans. Ind. Appl.*, vol. 58, no. 3, pp. 3696–3705, May 2022.
[18] H. Huang et al., "Sensorless control of permanent magnet in-wheel motor for EVs using global fast terminal sliding mode observer," *ISA Trans.*, vol. 160, pp. 186–195, May 2025.
[19] Q. Hou, S. Ding, and X. Yu, "Composite super-twisting sliding mode control design for PMSM speed regulation problem based on a novel disturbance observer," *IEEE Trans. Energy Convers.*, vol. 36, no. 4, pp. 2591–2599, Dec. 2021.
[20] J. Zhai and Z. Li, "Fast-exponential sliding mode control of robotic manipulator with super-twisting method," *IEEE Trans. Circuits Syst. II, Exp. Briefs*, vol. 69, no. 2, pp. 489–493, Feb. 2022.
[21] A. Nurettin and N. Inanç, "Sensorless vector control for induction motor drive at very low and zero speeds based on an adaptive-gain super-twisting sliding mode observer," *IEEE J. Emerg. Sel. Topics Power Electron.*, vol. 11, no. 4, pp. 4332–4339, Aug. 2023.
[22] C. Wang, L. Gou, S. Dong, M. Zhou, and X. You, "Sensorless control of IPMSM based on super-twisting sliding mode observer with CVGI considering flying start," *IEEE Trans. Transport. Electrific.*, vol. 8, no. 2, pp. 2106–2117, Jun. 2022.
[23] Y. He, Z. Cao, J. Mao, K. Liang, and C. Zhang, "Adaptive super-twisting sliding mode control with disturbance compensation for speed regulation of PMSM system," *IEEE Control Syst. Lett.*, vol. 8, pp. 3410–3415, 2024.
[24] K. Shao, J. Zheng, H. Wang, X. Wang, and B. Liang, "Leakage-type adaptive state and disturbance observers for uncertain nonlinear systems," *Nonlinear Dyn.*, vol. 105, no. 3, pp. 1–13, Aug. 2021.
[25] K. Shao, J. Zheng, R. Tang, X. Li, Z. Man, and B. Liang, "Barrier function based adaptive sliding mode control for uncertain systems with input saturation," *IEEE/ASME Trans. Mechatronics*, vol. 27, no. 6, pp. 4258–4268, Dec. 2022.
[26] P. Liang, F. Chai, K. Shen, and W. Liu, "Water jacket and slot optimization of a water-cooling permanent magnet synchronous in-wheel motor," *IEEE Trans. Ind. Appl.*, vol. 57, no. 3, pp. 2431–2439, May 2021.
[27] C. Du, C. Yang, F. Li, W. Gui, and W. Li, "Design and implementation of observer-based sliding mode for underactuated rendezvous system," *IEEE Trans. Syst., Man, Cybern., Syst.*, vol. 51, no. 10, pp. 6003–6014, Oct. 2021.
[28] B. Jiang, H. R. Karimi, Y. Kao, and C. Gao, "Takagi–Sugeno model-based sliding mode observer design for finite-time synthesis of semi-Markovian jump systems," *IEEE Trans. Syst., Man, Cybern., Syst.*, vol. 49, no. 7, pp. 1505–1515, Jul. 2019.
[29] K. Shao, J. Zheng, H. Wang, F. Xu, X. Wang, and B. Liang, "Recursive sliding mode control with adaptive disturbance observer for a linear motor positioner," *Mech. Syst. Signal Process.*, vol. 146, Jan. 2021, Art. no. 107014.
[30] J. Zhou, W. Zhang, H. Zhou, Q. Li, and Q. Xia, "Design of integral sliding mode guidance law based on disturbance observer," *J. Syst. Eng. Electron.*, vol. 35, no. 1, pp. 186–194, Feb. 2024.
[31] J. P. Mishra, X. Yu, and I. Boiko, "Frequency-response of non-singular terminal sliding mode control with actuators," *IEEE Trans. Circuits Syst. II, Exp. Briefs*, vol. 69, no. 3, pp. 1392–1396, Mar. 2022.
[32] E. Lu, W. Li, S. Jiang, and Y. Liu, "Anti-disturbance speed control of permanent magnet synchronous motor based on fractional order sliding mode load observer," *IEEE Access*, vol. 12, pp. 71716–71732, 2024.

Hao Huang received the B.S. degree in electrical engineering from Wuhan University, Wuhan, China, in 2016, and the M.S. and Ph.D. degrees in control engineering from Army Engineering University, Nanjing, China, in 2021.

From 2021 to 2022, he was an Assistant Researcher at the Military Institute of Electrical Science and Technology, Naval University of Engineering, Wuhan. Since 2023, he has been a Lecturer at Naval Aeronautical University, Qingdao. His research interests include power electronics and drives, control of electrical drives, and intelligent control.

Sai Wang was born in 1989. He received the M.S. degree in electrical engineering from Naval Aeronautical University, Qingdao, China, in 2013.

He is the author of four academic books and has published over ten articles. His research interests include artificial intelligence, equipment fault diagnosis, and intelligent control.

Chunfeng Yu was born in 1983. He received the M.S. degree in computer technology and applications from Qingdao University of Technology, Qingdao, China, in 2008.

He is currently an Associate Professor at Naval Aeronautical University, Qingdao. He is the author of four academic books and has published over ten articles. His research interests include artificial intelligence, equipment fault diagnosis, and intelligent control.

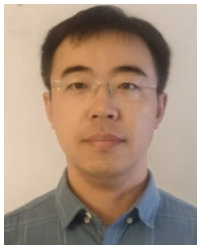

Zhonghua Sun received the M.S. degree in circuits and systems from the Air Force Early Warning Academy, Wuhan, China, in 2011.

He is currently a Lecturer at Naval Aeronautical University, Qingdao, China. His research interests include power supply systems, artificial intelligence, and electrical engineering.

Yuanfeng Zhang received the M.S. degree in electrical engineering from the Naval University of Engineering, Wuhan, China, in 2011.

He is currently a Lecturer at Naval Aeronautical University, Qingdao, China. His research interests include artificial intelligence, equipment fault diagnosis, and motion control.

Keqin Li (Fellow, IEEE) received the B.S. degree in computer science from Tsinghua University, Beijing, China, in 1985, and the Ph.D. degree in computer science from the University of Houston, Houston, TX, USA, in 1990.

He is a SUNY Distinguished Professor at the State University of New York, New Paltz, NY, USA, and a National Distinguished Professor at Hunan University, Changsha, China. He is a member at the SUNY Distinguished Academy and European Academy of Sciences and Arts, Salzburg, Austria.

Dr. Li is a fellow of AAAS, AAIA, ACIS, and AIIA.